

Development and testing of an all-additively manufactured hybrid thruster for smallsats

Abstract

Background: The design, development, and testing of a small-thruster system with additively-manufacturing key components is presented. The primary issue associated with conventionally-manufactured small thruster systems is the assembly complexity, where the motor case, injector, ignition electrodes, nozzle retainer, nozzle, fuel grain, insulating liner, and other components are fabricated individually and then assembled. For very small thruster systems, this detailed fabrication and assembly process is extremely labor intensive and time-consuming. Proposed “all-additive” designs reduce component fabrication and procurement cycle time, and may significantly reduce overall system complexity. Before committing to hardware, a student-lead design team reduced the trade-space to 2 design-options. Each option employs multiple additively-manufactured components including the oxidizer delivery system attachments, motor cap, motor casing, insulation, and the fuel grain. Components are additively manufactured using one of three different methods, fused-deposition modeling (FDM), stereo lithography (SL), and non-galvanic nickel plating (EN). Both designs feature an FDM-fabricated ABS fuel grain, with 1) a two material combustion chamber assembly fabricated from Veroclear® plastic using Polyjet 3-D SL printing technology, and 2) a chamber/fuel assembly additively fabricated from ABS, but plated with an external nickel coating. For simplicity the student prototype employs gaseous oxygen (GOX) and additively manufactured acrylonitrile-butadiene-styrene (ABS) as propellants. ABS has been previously demonstrated to be a highly efficient hybrid fuel material. The research campaign emphasized multiple objectives including hot and cold material testing burn lifetime survivability, system restart capability, and overall performance. Performance comparisons with hydrazine are presented.

Keywords: 3-D printing, hybrid rocket, additive manufacturing, electroplating plating, orbital debris mitigation

Volume 5 Issue 2 - 2021

Stephen A Whitmore

Department of Mechanical and Aerospace Engineering, Utah State University, USA

Correspondence: Stephen A Whitmore, Department of Mechanical and Aerospace Engineering, Utah State University, 4130 Old Main Hill, UMC 4130, Logan UT, USA, Postal Code 84322, Tel +1 (435) 760-0221, Email Stephen.whitmore@usu.edu

Received: July 23, 2021 | **Published:** August 10, 2021

Introduction

The recent growth of additive manufacturing technologies offers the potential to significantly change Material Acquisition methods for the Aerospace and Defense Industries. In typical aerospace applications using conventional manufacturing processes many required components are produced using “one-off” or very low volume production methods. These methods require the maintenance of expensive manufacturing facilities and assembly lines that can never recover the initial capital costs due to the very low required production rates.

Recently both the Department of Defense and NASA have initiated research directives that are investigating the use of modern computer-controlled robotic manufacturing methods to fabricate components additively; that is, components are built one-layer at a time from a base material. Modern additive manufacturing methods can support the production rates required for most Aerospace/Defense applications and offer the potential of improving low-volume component quality, consistency, and performance, while reducing development and production costs. Almost no residual material waste occurs using additive methods. Multiple vendors using these well-developed commercial technologies can produce identical pieces simultaneously, resulting in a “virtual assembly line.” These manufacturing advantages are not achievable using conventional methods.

In 2015 NASA concluded initial tests of the Space Launch System gas generator with the propellant injector 3-D printed using additive manufacturing technology.¹ A typical injector system is highly complex

and is very tedious to manufacture using conventional methods. Using additive methods took many hours off of the development and manufacturing time. In addition to injectors it is quite feasible for structural elements for the vehicle stage including aft skirt, nozzle enclosure, inter-stage structure, and all attachment and interface features required for the stage to also be “printed,” possibly as a single component. Multiple small businesses are currently thriving in the additive manufacturing market. If this capability is fully leveraged, the overhead of manufacturing a rocket no longer has to be carried by the Aerospace and Defense industries alone. The ability to “order” a rocket and have it manufactured and delivered in days to weeks versus months to years can revolutionize the space-launch market.

In fact, some “Futurologists” believe that 3D printing signals the beginning of a new style of manufacturing revolution, succeeding the production-line assembly that dominated manufacturing starting in the late 19th century.¹ Using the power of the world-wide-web it may eventually be possible to send a solid computer model of any product to any place in the world to be replicated by a 3D printer with “elemental inks” capable of being combined into any material substance of any desired form. This capability would duplicate the functions of the classical Star Trek “replicator.”

Background: review of additive manufacturing methods

Current production additive manufacturing methods include Electron Beam Manufacturing (EBM),² Selective Laser Melting

¹<http://3dprint.com/95914/nasa-3d-print-f1-rocket-engine/>

²https://en.wikipedia.org/wiki/Electron_beam_additive_manufacturing/

(SLM),³ and Direct Laser Metal Sintering (DMLS),⁴ for metallic components. Alternative methods known as Fused Deposition Modeling (FDM),⁵ Stereo Lithography (SL),⁶ and Polymer Injection (PolyJet®)⁷ are used to “print” plastic components. Each of the listed methods starts from a 3D computer-aided design (CAD) model that is constructed by the developing engineer or technician. Once the “build file” is completed, the model is downloaded to the machine’s processor, and the model is “sliced” into layers that are built-up up one level at a time. Most machines all the insertion of a soluble support structure as appropriate. Layers shapes are controlled in 3-dimensions by a computer numerically controlled (CNC) mechanism.

E-Beam is an older form of additive manufacturing technology that uses a high-wattage electron beam in a vacuum environment to melt the base metal powder layer by layer to create the part. More modern SLM methods replace the electron beam with a high power laser system. Both EBM and SLM methods create fully dense metal parts directly from metal powder with characteristics of the solid base material. DMLS technologies also employ a high-powered laser fired into a bed of powdered metal that is sintered together one-layer at a time to construct the 3-D shape. Although DMLS offers better component fidelity than either EBM or SLM, this sintering approach leaves small voids in the constructed material and the resulting structure is not fully dense. Both SLM and DMLS methods exhibit distinct advantages and disadvantages, depending upon the required application.

FDM is a 3-D printing method for thermoplastics, where a plastic filament is unwound from a coil and supplies material to a heated extrusion nozzle that heats the material to a near-liquid amorphous state. Once the material is layered-down, radiative cooling forms a solid material layer. SL uses photo-polymerization to links polymer chains together to form the component layers. This method requires an external ultraviolet light source to cure the material, PolyJet 3D printing is similar to inkjet printing, but instead of jetting drops of ink onto paper, PolyJet 3D Printers jet layers of curable liquid photopolymer onto a build tray where the layered materials are collected. FDM-built objects printed with thermo-polymers are fully recyclable and may be melted down and extruded to produce recycled feedstock. SL and PolyJet objects are not recyclable.

Hybrid rocket fuel grain production using additive manufacturing

Recently several research teams including Fuller et al.,² at Aerospace Corporation, Arnold et al. at Pennsylvania State University,³ and Whitmore and Peterson at Utah State University^{4,5} have demonstrated the effectiveness of using additive manufacturing techniques to fabricate plastic hydrocarbon fuel grains for hybrid rockets. These authors have demonstrated that using additive manufacturing hybrid fuel grains can be fabricated with an almost infinite range of fuel port shapes, allowing for significant enhancement of burn properties and combustion efficiencies. Of particular interest are helical fuel structures whose centrifugal flow patterns have been shown to significantly increase the fuel regression rate. Using a form of additive manufacturing known as Fused Deposition Modeling (FDM), Reference⁵ has printed fuel grains from ABS with embedded helical structures that have demonstrated a mean regression rate increase exceeding a factor of three. References^{2,3} have also successfully tested

³https://en.wikipedia.org/wiki/Selective_laser_melting/

⁴https://en.wikipedia.org/wiki/Direct_metal_laser_sintering/

⁵https://en.wikipedia.org/wiki/Fused_deposition_modeling/

⁶<https://en.wikipedia.org/wiki/Stereolithography/>

⁷<http://www.stratasys.com/3d-printers/technologies/polyjet-technology/>

acrylic hybrid rocket fuel grains with embedded swirl patterns that were additively manufactured using stereo-lithography.

Because FDM manufacturing builds the specimen one layer at a time, FDM-processed ABS possesses unique electrical breakdown properties that can be exploited to allow for rapid on-demand system ignition. Even though the ABS material possesses a very high electrical resistivity and dielectric strength and is not normally considered to be an electrical conductor; when FDM-processed ABS is subjected to a moderate electrostatic potential field, the layered material structure concentrates minute electrical charges that allow localized arcing between material layers. Joule heating from the resulting arc produces a small but highly conductive melt layer. This melt layer allows for very strong surface arcing to occur - even at moderate input voltage levels less than 200V- resulting pyrolysis of the surface fuel material. When this pyrolysis occurs in conjunction with the introduction of an oxidizer flow into the combustor, there exists a mixture of combustible gaseous and a source of activation energy (provided by the arc). This “seeded ignition” rapidly leads to self-sustaining combustion along the entire fuel port surface. On demand ignition has been demonstrated using both nitrous oxide (N₂O)⁶ and gaseous oxygen (GOX) as oxidizers.⁷

Original prototype 3-D printed hybrid rocket system

As mentioned in the introductory section, the additively manufactured thrust chamber was designed to act as a “drop-in” replacement for an existing, well-characterized hybrid motor. This original prototype rocket system was designed as a “green” alternative to replace existing hydrazine monopropellant space thruster systems. Additive manufacturing that lays down “horizontally-stacked” layers of the fuel grain material is an essential feature of this concept. The layering of the printed ABS enables and enhances the previously described arc ignition phenomenon. Identical ABS fuel segments made from extruded and machined ABS do not exhibit the previously described arcing properties and moderate voltage levels.

As described in detail by Refs.^{6,7} this seed-ignition concept has been developed into a power-efficient system that can be started and restarted with a high degree of reliability. Figure 1 shows an example of the additively manufactured grain with embedded electrodes. Multiple prototype devices based on this concept with thrust values ranging from 4.5 to 900 N have been developed and tested. All units are capable of multiple restarts and can be operated in either continuous or pulse modes, to replace hydrazine for many in-space propulsion applications.



Figure 1 Additively-manufactured fuel grain with embedded electrodes.

Figure 2 shows a 25 N flight-weight thruster during a recent static test-firing. Using gaseous oxygen (GOX) as the oxidizer and additively fabricated fuel sections made from commercially-available Stratasys ABSplus-340® feed-stock, the GOX/ABS thruster has achieved specific impulse values in excess of 220 seconds under ambient operating conditions. Results from “soft-vacuum” static test firings show that the achieved Isp exceeds 280 seconds.⁸

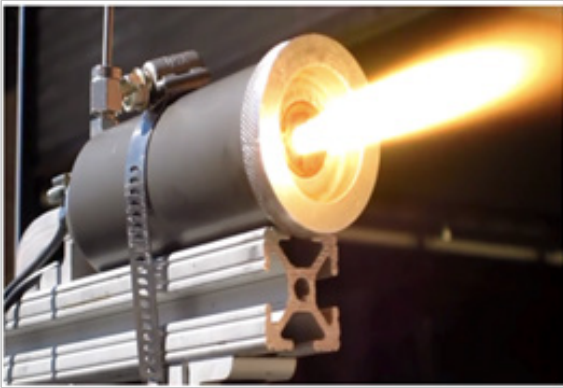


Figure 2 Static-test of flight-weight green thruster.

Based on verified Ballistic models of the system, the “hard-vacuum” I_{sp} extrapolates to greater than 300 seconds. This value exceeds monopropellant hydrazine I_{sp} performance level by more than 20%. This High Performance Green Hybrid Propulsion (HPGHP) performance enhancement is achieved by a comparably simple configuration layout with an inherently safe and environmentally sustainable system design. In fact, the current system offers the safety and environmental friendliness of a cold-gas system, but at a significantly higher performance level.

On March 25th, 2018 a flight experiment containing two counter-thrusting 10-N thruster prototypes of this thruster system was launched aboard a two-stage Terrier-Improved Malemute sounding rocket from Wallops Flight Facility (WFF). The launch achieved apogee of 172km, allowing more than 6 minutes in a true space environment above the Von-Karman line. During the mission the USU thruster was successfully fired 5 times in a hard vacuum environment. The payload section was successfully recovered by WFF flight support. Low-resolution telemetry data was successfully downlinked and delivered to USU for analysis. Whitmore and Bulcher⁹ report the details of this flight test experiment. Thus, with this spaceflight demonstration the technology readiness level (TRL) of the arc ignition technology must be acknowledged to be at least level 5.

“Drop-In” design for the additively manufactured thrust chamber

As described in the introduction section, one issue associated with the current system is the complexity of the component assembly, where the motor case, injector, ignition electrodes, nozzle retainer, nozzle, fuel grain, insulating liner, and fuel grains are fabricated or procured individually and then assembled by hand. The proposed “all-additive” design will reduce the component fabrication and procurement cycle time, and significantly reduce the overall system complexity.

As discussed previously, a student-lead senior design team was tasked to develop an additively-manufactured hybrid rocket thrust chamber that will act as a “drop-in” replacement for an existing thrust chamber of a small electrically-ignited hybrid rocket that uses gaseous oxygen (GOX) and acrylonitrile-butadiene-styrene (ABS) as

propellants. Students must design thrust chamber that incorporates pressure vessel, fuel, insulation, ignitor electrodes, and pressure seal/injector/nozzle interfaces as a single piece. “Add-in” components, nozzle, injector, end seals, etc can be conventionally manufactured or commercially procured. Design will replace existing 5-piece system, and was required to meet the following top-level criteria

- Thrust chamber must be 100% additively manufactured.
- Assembled system must integrate with the USU Propulsion Lab instrumentation and firing sequence control systems.
- Rocket must produce 10-25 N range of thrust.
- In order to ensure reliable arc-ignition, chamber pressure must operate in the range from 40-140 psig.
- Assembled system must hold up to 375-psig internal pressure under thermal load.
- Rocket must be restartable, and allow a minimum of 12 seconds of consecutive burn time with no structural or component failures, or motor burn-through.
- Delivered total impulse should exceed 200 N-seconds.
- Minimal oxidizer-to-fuel ratio (O/F) shift during burn lifetime.

System sizing analysis

Previous studies^{10,11} have demonstrated that the optimal performance oxidizer to fuel ratio (O/F) for GOX/ABS lies between 1.7 and 1.8 depending on the specific ABS formulation. Experimental results were also verified by calculations performed using the NASA equilibrium program “Chemical Equilibrium with Applications” (CEA).¹² The combustion chamber layout was sized using the classical Marxman enthalpy-balance regression rate model^{13,14} corrected for non-unity Prandtl number as previously developed by Eilers and Whitmore,¹⁵

$$\dot{r} = \left(\frac{0.0425}{\rho_{fuel} \cdot P_r^{0.377}} \right) \left(\frac{\Delta h_{flame/fuel}}{h_v} \right)^{0.565} G_{ox}^{0.8} \left(\frac{\mu}{L} \right)^{0.2} \quad (1)$$

In Eq. (1) \dot{r} is the mean longitudinal regression rate, G_{ox} is the oxidizer mass flux, L is the fuel port length, ρ_{fuel} is the fuel material density, μ and P_r are the mean viscosity and Prandtl number of the exhaust products, and $\frac{\Delta h_{flame/fuel}}{h_v}$ is the ratio of the convective heat transfer enthalpy to the enthalpy of vaporization of the fuel material. The combustion products were calculated from tables developed using CEA.¹² A mass balance across the combustor was used to size the injector and nozzle throat area for the desired mid-range chamber pressure level - approximately 80 psia, and the one-dimensional de Laval¹⁶ flow equations were used to optimize the nozzle exit area for the altitude of the test facility in Logan UT, approximately 1450 meters (4750 ft.) above mean sea level. The outer grain diameter is sized to allow an approximate 12-second burn lifetime at the maximum desired thrust level, 20 N. Table 1 shows the final parameter values for the main geometry components.

Trade study to select additively-manufactured motor assembly options

As described previously, a primary objective of this development campaign is the fabricate, integrate, and test an entirely additively manufactured combustion chamber assembly. A preliminary trade study was performed in which multiple criteria including fabrication

costs, ease of manufacturing, system weight, factors of redundancy, and motor ignition/restart capability were considered. Because motor restart capability is a primary consideration for this design, an extensive study was performed to assess the effectiveness of multiple commercially available 3-D printed materials for arc-ignition.¹⁷ Recall that the original motor design relies on the unique electrical breakdown properties of horizontally-layer, FDM-processed ABS to enable low-wattage, arc ignition without the use of pyrotechnic materials. The goal was to identify any commercially available 3-D printable materials that were equivalent or possibly superior fuel alternatives to ABS.

Table 1 Dimensions of major motor components

Fuel Port Bore Diameter	1.7cm
Fuel Grain Outer Diameter	3.3cm
Fuel Grain Length	8.8cm
Nozzle Throat Diameter	0.6cm
Injector Diameter	0.138cm
Nozzle Expansion Ratio	2.4:1

The ignition study tested specimens included photopolymers processed using PolyJet (stereo-lithography) and fused-deposition printing. Comparison metrics include general “arc-ability,” pyrolysis rate, dissipated power, characteristic velocity (C^*), and ability for multiple restarts. Initially, an ensemble of 8 commonly available “printable” polymers was evaluated, and only 4 printable materials - high- and low-density ABS, VeroClear®, and white polycarbonate - were found to possess effective “sparkling” properties. In follow-on burn tests only high- and low-density ABS and VeroClear performed effectively as fuel materials. White polycarbonate would not ignite using the arc-method. High-density ABSplus-340®⁸ exhibited the best overall ignition properties and characteristic velocity. Thus, the choice of fuel material was immediately constrained, and the primary design task for the student design team became the design of the additively manufactured thrust chamber pressure vessel.

The student design team reduced the trade-space to three design options 1) a 100% FDM-fabricated ABS combustion chamber assembly, 2) a two material assembly with an internal fuel component fabricated from ABS using FDM processing and an external pressure vessel fabricated from VeroClear® plastic using PolyJet technology, and finally 3) a motor assembly fabricated from FDM-processed ABS, but plated with an external nickel coating manufactured by a process known as “electroless plating” or auto-catalytic plating.⁹ This non-galvanic plating method involves several simultaneous reactions in an aqueous solution, and does not require the use of external electrical power for the plating reaction. Each of these design options will be summarized in the following sections.

ABS combustion chamber

ABS possesses several unique thermal and structural properties that make the consideration of a 100% plastic combustion chamber a viable option. First, printed ABS is a very strong and resilient material. ABS has a high tensile strength 40 MPa and a flexural strength of 75 MPa.¹⁰ This tensile strength is approximately 38% of the tensile strength of aluminum. Because ABS can be printed in any form or shape, regions of high stress concentration can be printed with additional material thickness to offset this load concentration. This

option does not exist with conventionally manufactured cylindrical pressure vessels.

Second, printed ABS possesses unique self-cooling properties. When ABS pyrolyzes an amorphous fluid-like layer is formed before vaporizing, and this layer allows for significant film cooling. Because this self-cooling property and the low thermal conductivity of ABS, virtually all of the heat of combustion is imparted to the exhaust plume and the fuel grain exterior does not heat up during the rocket burn. Not only does this property improve combustion efficiency; it also keeps the external surface of the fuel material cool. Figure 3 presents the results of an experiment that was performed with the original flight weight prototype thruster to verify this assertion.

Figure 3a shows the locations of three thermocouples (TCs) that were placed into the aft end of the fuel grain just ahead of the nozzle retainer. The inner TC was placed at a depth of $1/2$ motor radius into the fuel grain, a second TC was placed $1/4$ th of the radius into the grain, and finally, a third outer TC was placed in contact with the motor case. The motor was burned for 3 seconds, and temperatures were recorded for one hour to monitor soak back into the fuel grain structure. Figure 3b shows this result. During the burn, the motor is so well insulated that even the inner TC show no immediate response to the burn, even though models predict exhaust plume temperatures as high as 3000°C. After 10 minutes, the soak back temperature only rises to slightly less than 36°C, indicating that the vast majority of the combustion energy exits the motor via the exhaust plume.

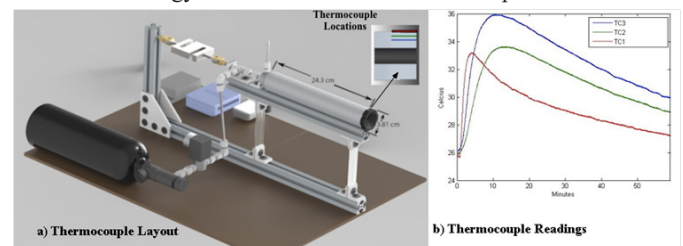


Figure 3 Printed ABS fuel grain internal temperatures following 3-second burn.

In fact, observations from previous FDM-ABS hybrid tests performed in the USU Propulsion Research Laboratory have shown that even after a 10 second burn the external thrust chamber casing remains comfortable to touch. Using FDM-processed ABS as a fuel material, external motor case temperatures have never been measured to exceed 50°C during testing. The self-cooling property of ABS does not exist with conventional thermo-setting propellant binders such as HTPB and PBAN. This cooling property allows the thrust chambers to be closely coupled with system avionics and other supporting structures without transferring the heat of combustion. Effects of heating loads on the outer layers of the fuel material can be considered as mostly negligible.

Thus, for this design consideration the relative strength and insulation properties of the ABS seeding material will be exploited to allow the fuel grain to support both the longitudinal launch loads and a significant portion of the combustion chamber pressure load. The primary design tasks are to print sufficient material thickness to support the required pressure loads and to ensure that the external surface of the material can be properly sealed so as to not allow slow lateral pressure leaks that would significantly impact performance.

Figure 4 shows a schematic of one concept where there is no distinct interface between the fuel and pressure vessel material. Once printed, the external surface of the material is sealed using solvents

⁸www.stratasys.com/materials/fdm/absplus/

⁹https://en.wikipedia.org/wiki/Electroless_plating/

¹⁰http://www.engineeringtoolbox.com/physical-properties-thermoplastics-d_808.html/

such as acetone or dichloroethane.¹¹ In this design option, threaded interfaces for the injector cap, chamber pressure transducer, and ignition electrodes are printed into the upper portion of the motor. A separate nozzle retainer is printed from ABS and fits onto the aft-end of the assembly. Details of the nozzle retention system are presented later in this section. If printed from the same feedstock material, then both pieces can be printed simultaneously.

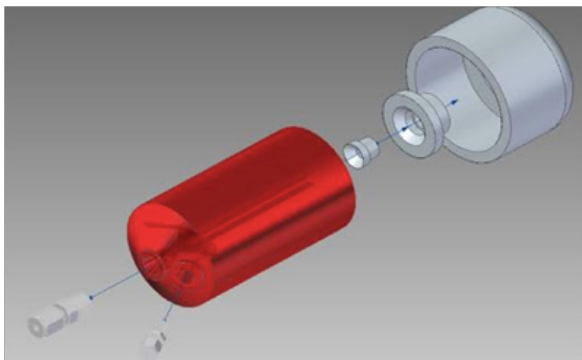


Figure 4 FDM-processed ABS thrust chamber assembly.

A clear advantage to the proposed design is manufacturing time and cost. With the proposed design is printed using the MAE department's in-house Stratasys Dimension 1200es¹² machine using ABSplus feed stock at a cost of \$6 per cubic inch, the entire cost of printing the required components is less than \$80. Other items associated with the motor assembly can be manufactured in-house at USU very minimal cost, making the total cost of the associated thruster system less than \$200. The associated time to build and assemble the required components is less than two working days.

The design of Figure 4, although being extremely easy and cost-efficient to manufacture, has several significant disadvantages. First, the design is not reusable at the end of the burn lifetime. Only the injector and pressure transducer fittings are salvageable. Second and most important, because the yield properties of the printed material under high heat and dynamic loads are not well understood, and the lower material strength of ABS when compared to metals - especially at higher temperatures - will require a considerably thicker wall compared to a metal thrust chamber. The result is a larger motor case and fuel weight - approximately 180grams, compared to 150grams for the original prototype. Because of the very low-associated cost of building the unit, the first limitation is only a minor disadvantage. The second shortcoming may eventually be overcome by detailed testing that identifies potential weak spots in the structure and builds additional support into the structure. It is also possible that the assembled structure will exhibit chaotic burn-to-burn characteristics that cannot be overcome with deterministic design modifications.

ABS/VeroClear combustion chamber

The second considered design is rather similar to the all-ABS chamber design, except that the fuel and thrust chamber shell are printed separately using different materials - ABS for the fuel grain and VeroClear® for the outer shell. Figure 5 shows the assembled motor and an exploded view of the layout. VeroClear® is a rigid, nearly colorless PolyJet photopolymer with proven dimensional stability for general purpose, fine-detail model builds. Here, VeroClear is preferred to ABS due to its better material properties with a tensile strength of greater than 60MPa, and flexural strength exceeding

85MPa. Also, with PolyJet printing technology the VeroClear shell has a smooth surface finish that provides a leak proof external seal. The lesser wall thickness results in reduced structural weight of 102 grams - approximately 47% lighter than the all-ABS design.

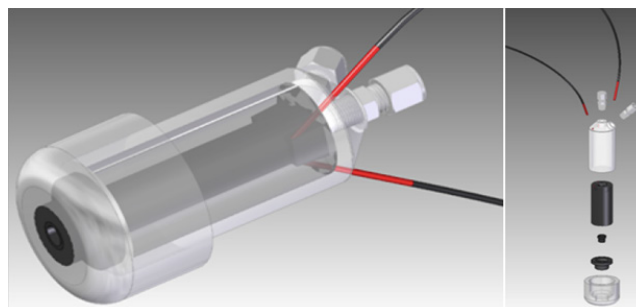


Figure 5 ABS/VeroClear thrust chamber assembly.

The two-material approach offers three distinct advantages, 1) a lower overall structural weight, 2) an "as-built" leak proof external shell, and 3) and potential reusability of the outer shell following the burn lifetime of the inner fuel grain. The primary disadvantage of this configuration is the need for two types of printer technology -- FDM and PolyJet - in order to fabricate the required components. Fortunately, the USU MAE department has access to both FDM and PolyJet technologies and the outer shell can be printed using an in-house Stratasys Objet30 Prime® machine.¹³ Because both printers can be operated simultaneously at the same cost, price and schedule impact for this design is considered to be identical to the all-ABS configuration.

Nickel-coated ABS combustion chamber combustion chamber

In the final design iteration, the thrust chamber is printed in a manner similar to the configuration of Figure 4; however, the printed configuration is nickel-coated using the previously described autocatalytic plating method. Figure 6 shows the assembled layout and an exploded view of the nickel-coated design. Plating the 3-D printed fuel material with a thin metallic film serves the purpose of sealing the grain from pressure leaks. The plating also significantly increases tensile strength, resulting in an extremely strong configuration.

Recent work performed at NASA Marshall Spaceflight center has demonstrated that additively-manufactured and nickel-coated ABS test specimens 2.5mm thick were able to withstand pressures in excess of 2000 psia. Hoop stress calculations predict typical thickness for nickel-plating between 4 mils and 10 mils (0.1mm - 0.25mm). Because of the load offset due to the nickel coating, the residual ABS wall thickness could be reduced to 6.25mm; resulting in by-far the lightest of the three motor prototypes to be developed. The estimated weight of the nickel-coated ABS chamber corresponds only 64 grams - less than 35% of the all-ABS thrust chamber design.

In a recently published work, Whitmore and Fehlberg¹⁸ have developed an inexpensive method for electroplating 3-D printed ABS. The USU-developed process involves the following steps; a) 3-D printing the base structure from ABS thermoplastic, b) sealing the surface to eliminate porosity - typically done with a combination of sanding followed by wiping with acetone, c) painting with an electro-conductive spray paint, d) direct copper electroplating, and finally e) nickel electroplating. This approach avoids the use of highly reactive and potentially dangerous, reagents like chromic and sulfuric

¹¹<http://nerfhaven.com/forums/topic/18527-intro-to-solvent-welding-plastic/>

¹²<http://www.stratasys.com/3d-printers/design-series/dimension-1200es/>

¹³<http://www.stratasys.com/3d-printers/design-series/objet30/>

acids, or hydrogen peroxide. This approach shows great promise and early structural testing shows that the resulting test articles are equally strong, when compared to the commercially produced test articles. However, this “home use” technology is rather immature, and the associated technical maturity level was insufficient allow hot fire testing for this project. All of the nickel-plated thrusters used for this testing campaign were commercially produced. The need for commercial out-sourcing was the primary disadvantage of the electroplated thruster design.

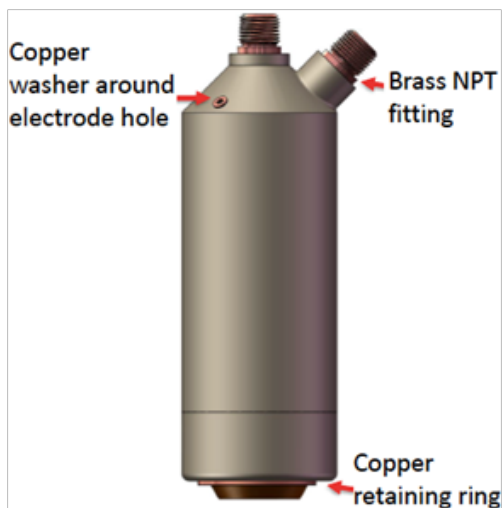
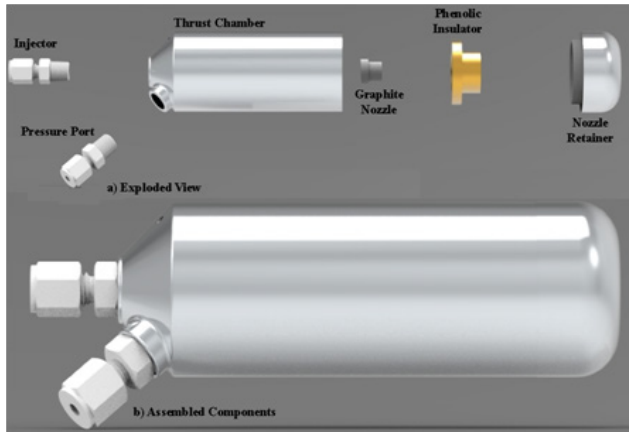


Figure 6 Nickel-plated ABS thrust chamber design.

Conventional industrial plating of thermoplastic materials like ABS involves a multistep process.¹⁹ First, electroless plating is often used to deposit copper on the surface of the substrate before nickel can be electroplated on the copper. Electroless plating generally involves the use of water-based solutions, but ABS is very hydrophobic. Commercial plating companies generally use strong acids, such as chromic and sulfuric acids, to etch the surface, and then activate the surface with nanoparticles of tin and palladium in solution to provide a catalyst for the electroless plating process. A copper-based solution is then applied to create a conductive coat, and nickel is electroplated onto the copper. This process is complex, potentially hazardous without proper controls, and *very* expensive. Even “environmentally friendly” methods^{20,21} still require use of concentrated sulfuric acid, hydrogen peroxide, and other expensive and hazardous chemicals to etch and seed the surface for electroplating.

Typical costs for a nickel-phosphorous alloy coating ranges from \$6.5-\$20 per cm²·mill.¹⁴ The current design has a surface

¹⁴<http://www.sharrettsplating.com/electroless-nickel-coating-metals/>

area of approximately 75cm²; thus a 4-mil coating would run from approximately \$300-\$900, substantially adding to the overall cost of the motor system. Because the cost of this system is substantially higher than the all-ABS design, lack of reusability is a significant drawback. However, for perspective it must be noted that the estimated nickel-plated motor cost varying from \$500-\$1000 each is still significantly less expensive than current conventional designs. This cost is compared to a similarly sized Aerojet 22-N hydrazine thruster is listed at more than \$250,00 delivered cost.¹⁵

Nozzle retainer

The components of the nozzle retainer system - shown in detail by Figure 7 - were designed with simplicity in mind. For each of the three proposed configurations the nozzle and phenolic insulator pieces are identical. However, for each design the printed retention caps have varying outside diameters and overlap onto the upper fuel grain section. The retention cap has two main functional requirements; 1) ensure the stability of the phenolic insulator and nozzle, and 2) hold the rocket together longitudinally when firing. The phenolic piece of the retainer is included to insulate the plastic retention cap from the super-heated nozzle. The bonding lip allows the retainer to be secured to the rocket motor shell. For the VeroClear combustion chamber design, this lip was manufactured as a separate piece. For the ABS chambers, the bonding lip was built into the fuel grain section.

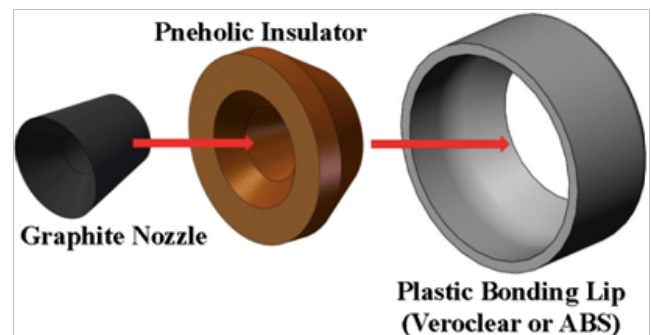


Figure 7 Detail of nozzle retention system.

The phenolic nozzle retainer and graphite nozzle are fabricated using conventional methods and bonded using high temperature adhesive. Several adhesive options for bonding the nozzle retainer to the upper fuel grain material were considered. These adhesives are Hysol E-40HT16 and a 3M Scotch-Weld 2216 Space Grade Epoxy¹⁷. All three materials were evaluated for static loads and heat resistance, and it was discovered that 3M Scotch-Weld 2216 had superior properties. This bonding agent was used throughout the testing to be presented in this paper. Figure 5 shows the end cap bonded onto the VeroClear thrust chamber shell.

Motor cap injector end-cap and pressure fittings

For this design, the injector end-cap is made of much weaker material than the current aluminum end-cap used by the conventional motor design. Thus the material dimensions must be significantly changed so the material does not fail under pressure. To account for this lower material strength, the material thickness between all holes in the end cap must be greater than the required wall thickness obtained from the pressure vessel calculations presented previously.

In the existing aluminum design, the pressure transducer fitting comes in at a right angle to the fuel grain. This bend prevents excess

¹⁵<https://www.rocket.com/propulsion-systems/monopropellant-rockets/>

¹⁶<https://tds.us.henkel.com/NA/UT/HNAUTTDS.../EA%20E-40HT-EN.pdf/>

¹⁷www.farnell.com/datasheets/692030.pdf/

radiation heat from impinging onto the transducer diaphragm. This layout requires a perpendicular hole to the long axis of the rocket. Since the casing will be printed from the bottom up, this will mean a horizontal hole will need to be printed to match the current design. When printing a hole in a material, 3D printers have diminishing accuracy issues as the hole becomes more horizontal. As a compromise between print accuracy and radiant heat deflection, this transducer access hole was placed at 45 degrees from the horizontal for the VeroClear model, and 60 degrees from horizontal for the ABS configuration (to allow support material removal). Figure 8a shows the printed injector end-cap layouts.

As shown by Figure 8b, 1/4" and 1/8" NPT pipefittings from the existing motor design were used to interface the injector and pressure port to the fabricated threads. Since the motor injector cap is made from printed plastic materials, the design of the external fitting threads represents a significant failure point. Prior to printing, design calculations were performed to ensure sufficient margin to mitigate any potential thread failures. The shear area for an internal thread is

$$A_n = \pi \cdot n \cdot L_e \cdot D_{s,\min} \left[\frac{1}{2 \cdot m} + 0.57735 \cdot (D_{s,\min} - E_{m,\max}) \right] \quad (1)$$

In Eq. (1) A_n is the shear area, $E_{n,\max}$ is the maximum pitch diameter of the internal thread, $D_{s,\min}$ is the minimum major diameter of the external thread, L_e is the thread engagement length, and n is the number of threads per inch. The required A_n to withstand the shear force generated by the chamber pressure is calculated by dividing the chamber pressure by the yield strength of the material. The engagement length is found using the known dimensions for the threads of the selected fitting. Assuming a safety factor of 5, a standard $M8 \times 0.8$ pipe fitting thread, and a strength of 55MPa, the calculated engagement length to prevent shearing at the root threads is 0.66mm. To account for the fact that this calculation assumes the printed material is isotropic, and that the threads are printed to exact dimensions, the printed hole was coated with Scotch-Weld 2216 before the threads were inserted to permanently bond the fittings to the motor case.



Figure 8 3D printed injector end cap schematics.

The top end of the motor will remain cool throughout the burn; so thermal expansion or thermal-load material weakening issues associated with the printed material threads should not be an issue. Should the plastic threads prove to provide insufficient support, an option exists to print slightly enlarged threads, and then bond the injector and pressure port NPT plugs directly to the cap material. Characterizing the performance of the printed threads was a key issue investigated during the testing campaign.

Arc-ignition electrode interface to injector cap

As described previously in this report, the arc-ignition system is a major feature of the proposed design, and the electrode interface to the injector cap is a key component of the system design. Figure 9 shows the electrode interface for the conventional thruster configuration, and Figure 10 shows the electrode interface for the fully 3-D printed thruster. Since typical ignition power demand is less than 10 watts, 18-gauge insulated solid copper wire is sufficient to carry the required ignition current. Printed holes in the fuel grain/motor cap allow access

of these wires to a pre-combustion chamber shelf built into the fuel grain material. The wires are bonded and sealed using one of the two previously described high-temperature bonding agents.

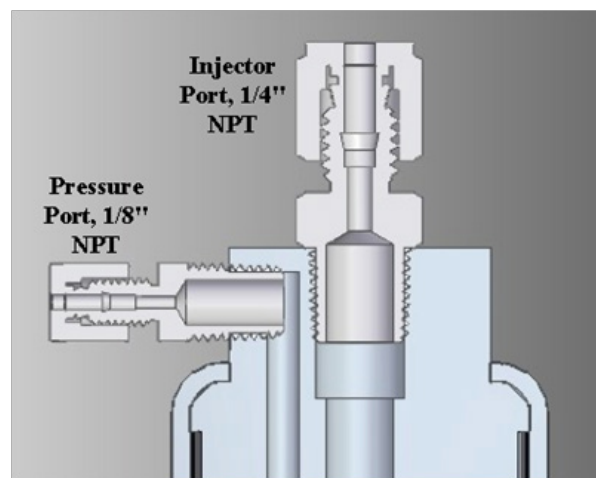


Figure 9 Existing motor cap fittings for standard flight weight, green propellant, thruster.

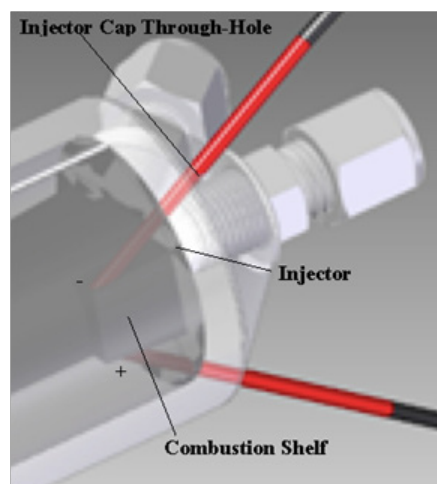


Figure 10 Electrode interface to printed motor cap.

Structural testing of thrust chamber samples

A series of static load tests were performed in order to verify the design stress calculations, and to ensure that the thrust chambers could safely withstand the loads imparted during the motor hot firing. A series of test articles identical to the previously described thrust chamber geometries with no nozzle exit were printed. These articles were tested using tap water pressurized via a manual hydrostatic pump. The load pressure was recorded using a gauge mounted to the pump, and the motor surface strains were measured using strain gauges mounted across and along the longitudinal axes. The following three sections summarize the static-test results.

Sealed ABS test article

This test article consisted of printed ABS with and without a coating of ABS glue to seal the material surface. Figure 11 shows this test article. The result was entirely unsatisfactory, as the chamber began to “seep” at pressures as low as 50 psig. Several attempts at sealing the surface were performed, but could not eliminate the seepage. The printed ABS material is simply inconsistent with stand-alone pressure vessel applications. Because of this result, a pure ABS

motor was no longer considered as viable, and this configuration was eliminated from follow-on testing.



Figure 11 Sealed ABS test article.

VeroClear shell test article

Because the inner ABS fuel is highly porous, conservatively, it was assumed that the VeroClear shell supports the entire pressure load of the thrust chamber. A conventional thick-walled cylinder stress analysis¹⁹ was used to calculate the required pressure vessel wall thickness for the VeroClear. Here the wall thickness is calculated as

$$\tau_{wall} = r \cdot \frac{\sqrt{\left(\frac{Y_s}{SF} - P_0\right)^2 + 2 \cdot P_0 \cdot \left(\frac{Y_s}{SF} - P_0\right)} - \left(\frac{Y_s}{SF} - P_0\right)}{\left(\frac{Y_s}{SF} - P_0\right)} \quad (2)$$

In Eq. (2) τ_{wall} is the wall thickness, Y_s is the yield strength of the material, P_c is the chamber pressure, and r is the internal diameter of the load-supporting wall. This analysis assumes a constant material temperature, which given the discussion of the previous subsection and the data presented by Figure 3, appears to be a reasonable assumption. Table 2 shows the wall geometry, material properties, and calculated wall thickness for the VeroClear shell.

Test article geometry

The initial VeroClear test article was printed with a mid-range of the calculated shell wall thickness of 4 mm, and second article was printed with a significantly thinner shell of 2mm. In order to avoid a noted potential problem with a stress concentration at the 90-degree bend where the pressure vessel and cap meet, the original design of Figures 4 and 5 was re-engineered to allow the end cap to fit inside of the motor shell. A tapered 5mm fillet was inserted where the end

Table 2 Calculated wall thickness dimensions for the proposed materials

Pressure Vessel Wall Material	Inner Radius of Support Wall, mm	Internal Chamber Pressure, Psig	Tensile Strength of Material, Mpa	Factor of Safety	Wall Thickness mm
VeroClear	16.385	375	50-65	5	3.66-4.96

Table 3 Summary of structural test article geometries

Test Article	Nickel Plating Thickness, mil	Internal Port Diameter, mm	ABS Wall Thickness, mm	No of Specimens Tested
1	4	32.77	3.81	3
2	4	32.77	8.41	2
3	16	32.77	3.18	2
4	16	32.77	8.41	1

Estimating the plated material structural properties

Because of the material bonding between the ABS fuel and the external nickel plating, the structural analysis of this design was

cap intercepts the motor shell, and the end cap was tapered with a 5mm radius. The end cap was glued to the main shell using the previously described bonding agent. This re-design has the advantage of a constant diameter external motor mold line.

Pressure test results

Interestingly, both the 4-mm and 2-mm wall thickness test articles failed at nearly the same pressure level, 558 and 567 psig respectively. For both cases the failure point was along radius of the end cap at the stress concentration point where the 5mm radius is located. Figure 12 compares the 4mm wall thickness test article before and after load testing. It is apparent that wall thickness doesn't play as large an issue for the pressure vessel test as the stress concentration of the 5mm fillet. Although both pressure vessels well exceeded the 375-psi ultimate chamber pressure requirement, as an additional precaution the 5mm radius was changed to a 10mm radius on both the nozzle retention cap and the end of the motor casing. Both the thick and thin-wall pressure vessels were carried forward for hot-fire testing.

Nickel plated ABS test article

Because the ABS fuel material will carry some of the structural load in addition to the nickel surface coating, four different nickel-plated test articles were evaluated during static load testing. The structural test specimens were for the nickel-plated thruster chambers designed identically to the thrust chamber pictured by Figure 6, except the bottom end was printed with a closed end and no nozzle insert was installed.

Test article geometry

Figure 13 shows the structural layout of the 3-D printed ABS test structure. As summarized by Table 3 the nickel-plated structural test articles were printed with 4 different configurations; these were 1) a thick walled ABS grain (8mm) with a 4-mil nickel coating, 2) a thin walled ABS grain (5.4mm) with a 4-mil nickel plating, 3) a thick walled ABS grain (10.1mm) with a 16-mil nickel coating, and 4) a thin walled ABS grain (4mm) with a 16 mil nickel plating. The thick and thin ABS walls represent the motor casing at the beginning of the burn and later into the burn when the fuel grain has receded. For all test articles the internal port diameter was fixed at 32.77mm, and the wall thickness was varied by increasing the outer diameter of the test specimen. The thick and thin ABS walls were designed to simulate the internal motor configuration at the beginning of the burn and later into the burn when the fuel grain has receded. The selected nickel plating thickness, but allowed a wide range to be investigated.

significantly more complex. Here the values for the Elastic modulus and Poisson's ratio (E, ν) were estimated using the law of volumes.²³ Assuming the nickel plating and ABS wall lengths are roughly

the same dimension, the elastic modulus of the plated material is approximately,

$$E_{total} = \frac{E_{ABS} \cdot V_{ABS} + E_{nickel} \cdot V_{nickel}}{V_{ABS} + V_{nickel}} = \frac{E_{ABS} \cdot [(r_{inner} + t_{wall})^2 - (r_{inner})^2]_{ABS} + E_{nickel} \cdot [(r_{inner} + t_{wall})^2 - (r_{inner})^2]_{nickel}}{[(r_{inner} + t_{wall})^2 - (r_{inner})^2]_{ABS} + [(r_{inner} + t_{wall})^2 - (r_{inner})^2]_{nickel}} \quad (3)$$

$$= \frac{E_{ABS} \cdot [t_{wall} \cdot (2 \cdot r_{inner} + t_{wall})]_{ABS} + E_{nickel} \cdot [t_{wall} \cdot (2 \cdot r_{inner} + t_{wall})]_{nickel}}{[t_{wall} \cdot (2 \cdot r_{inner} + t_{wall})]_{ABS} + [t_{wall} \cdot (2 \cdot r_{inner} + t_{wall})]_{nickel}}$$

For the nickel plating, the approximation $2 \cdot r_{inner} \gg t_{wall}$ is introduced and Eq. (3) reduces to,

$$E_{total} = \frac{E_{ABS} \cdot [t_{wall} \cdot (2 \cdot r_{inner} + t_{wall})]_{ABS} + E_{nickel} \cdot [t_{wall} \cdot (2 \cdot r_{inner} + t_{wall})]_{nickel}}{[t_{wall} \cdot (2 \cdot r_{inner} + t_{wall})]_{ABS} + [t_{wall} \cdot (2 \cdot r_{inner} + t_{wall})]_{nickel}} \quad (4)$$

Since $(r_{inner})_{nickel} = (r_{inner} + t_{wall})_{ABS}$, Eq. (5) reduces to,

$$E_{total} = \frac{E_{ABS} \cdot t_{wall_{ABS}} \cdot (2 \cdot r_{inner_{ABS}} + t_{wall_{ABS}}) + E_{nickel} \cdot 2 \cdot (r_{inner_{ABS}} + t_{wall_{ABS}}) \cdot t_{wall_{nickel}}}{t_{wall_{ABS}} \cdot (2 \cdot r_{inner_{ABS}} + t_{wall_{ABS}}) + 2 \cdot (r_{inner_{ABS}} + t_{wall_{ABS}}) \cdot t_{wall_{nickel}}} \quad (5)$$

$$E_{ABS} \cdot \left(1 + \frac{1}{2} \cdot \left(\frac{t_{wall}}{r_{inner}}\right)\right) + E_{nickel} \cdot \left(1 + \left(\frac{t_{wall}}{r_{inner}}\right)\right) \cdot \left(\frac{t_{wall_{nickel}}}{t_{wall_{ABS}}}\right)$$

$$\left(1 + \frac{1}{2} \cdot \left(\frac{t_{wall}}{r_{inner}}\right)\right) + \left(1 + \left(\frac{t_{wall}}{r_{inner}}\right)\right) \cdot \left(\frac{t_{wall_{nickel}}}{t_{wall_{ABS}}}\right)$$

In Eq. (5) the Elastic modulus of the plated material is a function of the elastic modulus of the component materials (nickel and ABS), and the ABS wall thickness to the inner ABS fuel port radius, and the ratio of the nickel plating thickness to the ABS wall thickness. Similarly, the Poisson's ratio is estimated by,

$$v_{total} = \frac{v_{ABS} \cdot V_{ABS} + v_{nickel} \cdot V_{nickel}}{V_{ABS} + V_{nickel}} = \frac{v_{ABS} \cdot \left(1 + \frac{1}{2} \cdot \left(\frac{t_{wall}}{r_{inner}}\right)\right) + v_{nickel} \cdot \left(1 + \left(\frac{t_{wall}}{r_{inner}}\right)\right) \cdot \left(\frac{t_{wall_{nickel}}}{t_{wall_{ABS}}}\right)}{\left(1 + \frac{1}{2} \cdot \left(\frac{t_{wall}}{r_{inner}}\right)\right) + \left(1 + \left(\frac{t_{wall}}{r_{inner}}\right)\right) \cdot \left(\frac{t_{wall_{nickel}}}{t_{wall_{ABS}}}\right)} \quad (6)$$

Estimating the wall stresses

The wall stresses were evaluated using were estimated using thick-wall cylinder theory, where at the outside wall, the corresponding hoop (σ_H) and axial (σ_L) stresses are,

$$\sigma_H = 2 \cdot P_c \cdot \frac{r_{inner}^2}{(r_{outer} + r_{inner}) \cdot (r_{outer} - r_{inner})} = 2 \cdot P_c \cdot \frac{r_{inner}}{\left(2 + \frac{t_{wall}}{r_{inner}}\right) \cdot t_{wall}}$$

$$\sigma_L = P_c \cdot \frac{r_{inner}^2}{(r_{outer} + r_{inner}) \cdot (r_{outer} - r_{inner})} = P_c \cdot \frac{r_{inner}}{\left(2 + \frac{t_{wall}}{r_{inner}}\right) \cdot t_{wall}} \quad (7)$$

In Eq. (7) the r_{inner} is the inner ABS port diameter (32.77 mm), t_{wall} is the total wall thickness ($t_{ABS} + t_{nickel}$), and P_c is the internal test (or chamber) gauge-pressure.

Structural testing of the nickel plated abs test articles

Each of the stress-tests tabulated by Table 3 were completed, with a total of 8 tests completed. The structural test articles were dynamically tested in a hydrostatic test unit where the interior pressure of the test article was cycled multiple times from approximately slightly greater than 100 psig to 1000 psig. Strain gauges aligned in the parallel to the axial and longitudinal axes were mounted near the center of the test article in order to capture the hoop and axial deformations during testing. Figure 14 plots a typical time history trace obtained from a test of the thin walled-ABS test article with 4-mil nickel coating. Plotted as a function of time are the 14(a) hoop strain (ϵ_H), 14(b) axial strain (ϵ_L), and 14(c) internal gauge-pressure, P_o . Finally, strain-pressure cross plots and associated curve-fits are plotted by Figure 14. Here Fig. 14(d) plots hoop strain vs. pressure, Fig 14(e) plots axial strain vs. pressure.

Since, the combined Elastic Modulus and Poisson's ratio for

the plated material can be written as a function of the hoop and longitudinal stresses and strains,

$$E = \frac{\sigma_L^2 - \sigma_H^2}{\epsilon_L \cdot \sigma_L - \epsilon_H \cdot \sigma_H}$$

$$v = \frac{\epsilon_L \cdot \sigma_H - \epsilon_H \cdot \sigma_L}{\epsilon_L \cdot \sigma_L - \epsilon_H \cdot \sigma_H} \quad (8)$$

Substituting Eq. (7) into Eq. (8), noting that from Eq. (7) that $\sigma_H = 2 \cdot \sigma_L$ and simplifying, the combined value for the elastic modulus is

$$E_{combined} = \frac{3 \cdot \sigma_L}{2 \left(\epsilon_H - \frac{1}{2} \epsilon_L\right)} = \frac{3 \cdot P_c}{2 \left(\epsilon_H - \frac{1}{2} \epsilon_L\right)} \cdot \frac{r_{inner}}{\left(2 + \frac{t_{wall}}{r_{inner}}\right) \cdot t_{wall}} = \frac{3}{4} \cdot \frac{P_c \cdot r_{inner}}{\left(\epsilon_H - \frac{1}{2} \epsilon_L\right) \left(1 + \frac{1}{2} \cdot \frac{t_{wall}}{r_{inner}}\right)} \quad (9)$$

The corresponding value for Poisson's ratio is

$$v_{combined} = \frac{\epsilon_L - \epsilon_H \cdot \frac{\sigma_L}{\sigma_H}}{\epsilon_L \cdot \frac{\sigma_L}{\sigma_H} - \epsilon_H} = \frac{\epsilon_L - 2 \cdot \epsilon_H}{2 \cdot \epsilon_H - \epsilon_L} \quad (10)$$

The total composite wall thickness includes both the ABS and nickel plating thicknesses. Using the data from Figs 14(d) and 14(e), and Eqs. (9) and (10), the estimated the Elastic Modulus and Poisson ratios are calculated. Figure 15 plots those estimates as a function of the chamber pressure. The corresponding uncertainties based on the curve fit root-mean-square (RMS) errors are also plotted.

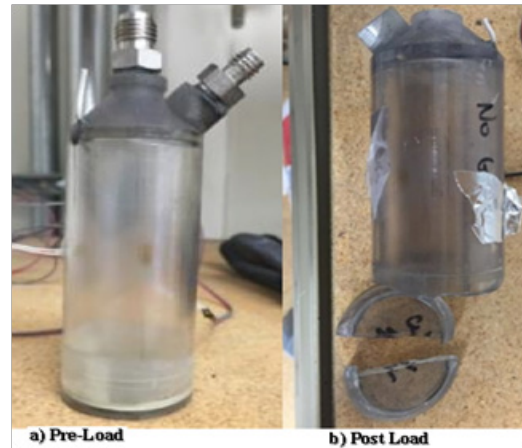


Figure 12 VeroClear chamber, pre- and post-load test.

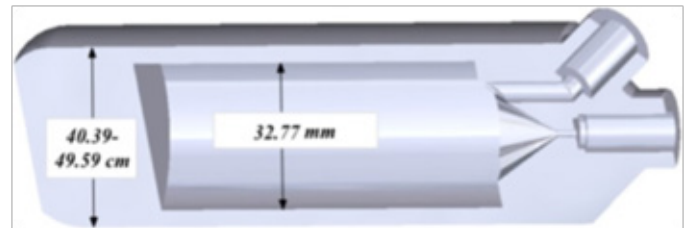


Figure 13 Layout of 3-D ABS structure for pressure testing.

The previously-described method of Eqs. (5) - (10) was subsequently used to calculate the material properties (E , v) for each of the test articles of Table 3. Figure 16 summarizes those results. The data from Table 3 are plotted as the red (16-mil nickel plating) and black (4-mil nickel plating) symbols, with the thin solid red and black lines representing a linear curve fit of the data. The dashed lines representing the curve-fit uncertainty. The thick solid red and black lines represent the Elastic Modulus and Poisson's ratio as calculated

from the law of volumes, Eqs. (5) and (6). For these calculations, the assumed material properties for nickel²⁴ and ABS²⁵ were $\{E, \nu\}_{ABS} = \{2.35 \text{ GPa}, 0.40\}$ and $\{E, \nu\}_{nickel} = \{203 \text{ GPa}, 0.31\}$, respectively. The wall thickness, plotted on the abscissa includes the thickness of both the ABS web and the nickel plating. The data from Figure 16 present a “sanity-check” structural test results.

The thick wall ABS, 4-mm nickel coated test article failed along the entire length of the motor at approximately 585 psi. Figure 17 shows the 4-mil, thick ABS test article pre-and post-failure. The remaining test articles survived up to the load capacity of the test setup - approximately 1000 psig. Since all of the test articles featured the same external diameter, it is likely that the thick walled 4-mil test article failed due to hoop stress concentrations resulting from the smaller internal radius of the ABS grain. In all cases the test articles exceed the required 375-psig ultimate load limit and were carried forward for hot-fire testing.

The 16-mil coated test specimens exhibit anomalously high elastic modulus when compared to the “theoretical” prediction, indicating that the surface bond of the plated material adds strength above and beyond their composite properties. The ABS wall thickness appears to have only a small effect upon the strength of the test article. The Law of Volumes analysis does predict the counter- intuitive declining

material strength as a with increasing ABS wall thickness. In fact, during static testing one of the 4- mil, thick wall test articles failed along the entire length of the motor at approximately 600 psig load pressure. All of the other test articles, including the 4-mil, thin walled test articles survived to pressures greater than 1000 psig without yield.

Hot-fire testing of thrust chambers

Tables 4 and 5 summarize the test matrix, and the overall test results. Detailed results for each motor are presented in subsequent sections. As described in the previous section, multiple printed motor designs were cleared during static- load testing and deemed to be safe to carry forward for hot fire testing. Both the thick (4mm - 2 motors tested) and thin walled (2mm - 1 motor tested) variants of the VeroClear design were tested. Because of the case sidewall failure of the thin-wall Nickel-coated thrust chamber during static testing, only the thick wall (16mil) Nickel Plated motor was tested during the hot-fire campaign. The VeroClear motors were tested first, followed by the nickel-plated motor. Primary objectives of the tests were to establish the end-to-end survivable burn time, demonstrate the restart capability, and assess the system total impulse, thrust, and specific impulse (I_{sp}) values. The initial ABS fuel grain wall thickness for each test was 15mm for each motor.

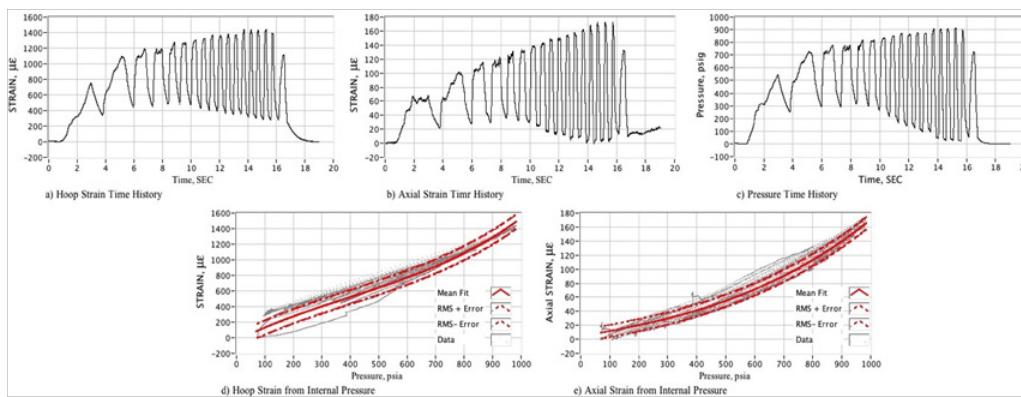


Figure 14 Typical nickel-plated structural test article load-response time history.

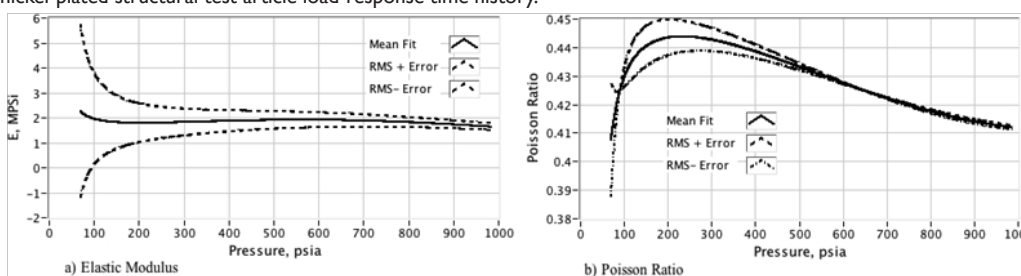


Figure 15 Elastic modulus and Poisson ratio estimated from longitudinal and axial strain measurements.

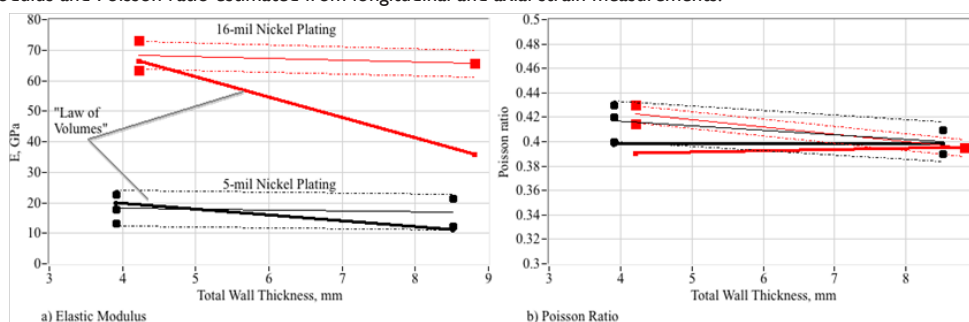


Figure 16 Elastic modulus and Poisson ratio estimates plotted vs. total wall thickness.

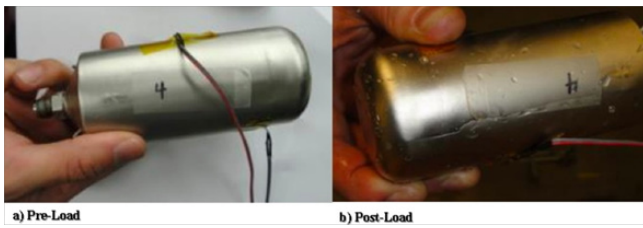


Figure 17 Nickel-plated abs chambers, pre- and post-test images showing longitudinal wall fracture.

The specific impulse for each motor was calculated by dividing the total delivered impulse by the amount of propellant consumed up to the point of failure. Due to a higher operating chamber pressure, the VeroClear motors exhibited a slightly higher specific impulse than did the Nickel-plated motors. The reasons for this higher chamber pressure will be discussed later in Section J. The listed vacuum specific impulses in Table 3 are projections based on nozzle throat conditions with the motor operating in a vacuum and an assumed 25:1 expansion ratio nozzle. Although the VeroClear motors exhibited slightly higher I_{sp} in the lab due to the better-optimized nozzle expansion ratio at the operating chamber pressure, the projected vacuum specific impulse of both systems are roughly equivalent. Only the nickel-plated motor survived the desired 12-second cumulative burn lifetime. The thick walled Nickel-Plated rocket weighed approximately two times greater than the thick-walled VeroClear-rocket.

Test apparatus

The motors were interfaced to an existing test stand originally designed for the conventionally manufactured thruster configurations. Figure 18 shows the test stand layout, and Figure 19 shows the Piping and Instrumentation Diagram (P&ID) of the test systems. Measurements included thrust, chamber pressure, oxidizer massflow, pre- and post-fuel weights, and thermocouples on the midpoint and aft end of the motor case. All tests were performed in Utah State University’s on-campus test cell located in the Engineering Technology Building. Two National Instruments data acquisition and control devices manage the automated motor fire control, and test data logging. Operators and experimenters are remotely located in a secure control room separated from the test area. Communications to the test stand are managed by an operator-controlled laptop running the LabVIEW programming language via universal serial bus (USB) using amplified extension cables.

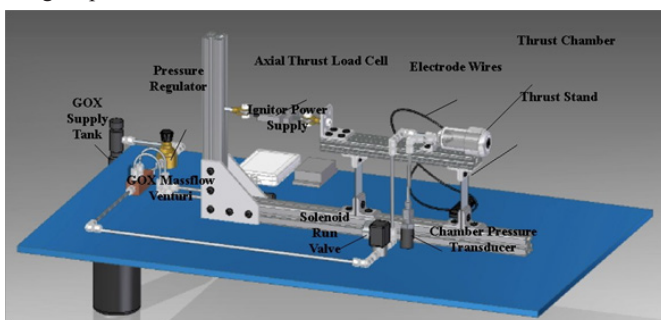


Figure 18 Schematic of the thrust stand and additively manufactured test motor.

Finally, Figure 20 shows the signal flow control diagram of the motor ignition and control system. The ignition spark and power is provided by a 60W, 15V power supply. Depending on the impedance on the arc path between the ignitor electrodes, the low voltage is raised to

250-1000 V, current limited at 6 mA by the UltraVolt D-series voltage amplifier, and this unit provides the inductive ignition spark that also pyrolyzes sufficient ABS material to seed ignition. The current setup was pre-programmed for the ignition spark to lead the GOX valve opening by 500 msec, and terminated 500 msec after the GOX valve opening. The ignition spark lead and post GOX valve termination time is a programmable user control setting. Once initiated, full combustion typically occurs very rapidly, less than 200 msec.

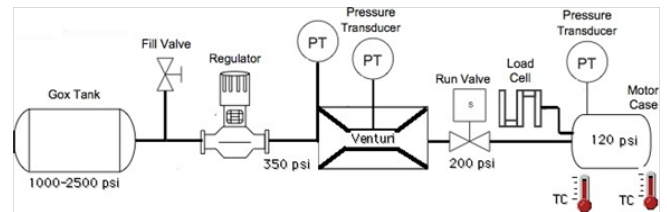


Figure 19 Piping and instrumentation diagram of test apparatus.

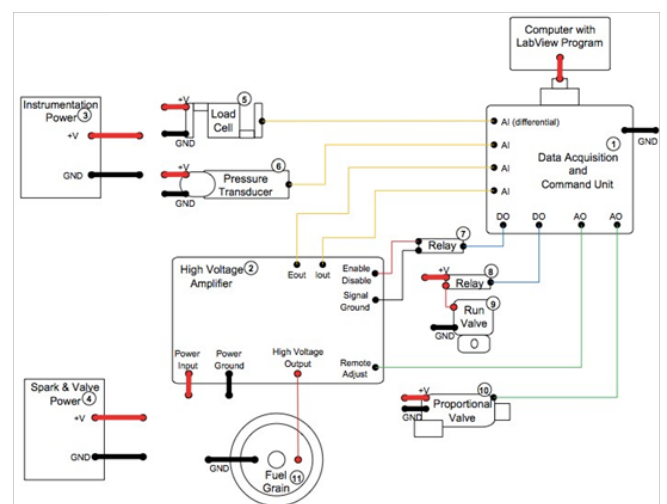


Figure 20 Ignition system signal flow diagram.

Although inline Venturi allows measurements of the oxidizer mass flow in real time, the test stand does not allow for motor fuel-consumption mass measurements in real time. Thus, for this testing campaign, each grain was burned multiple times to allow intermediate mass measurements to be obtained by removing the motor from the test stand and measuring the interim weight between burns. The fuel mass flow was calculated as the difference between the measured oxidizer mass flow and the nozzle exit mass flow. The nozzle exit mass flow was calculated based on the measured chamber pressure, flame temperature, nozzle exit area, and exhaust gas properties using the 1-dimensional choking mass flow equation,

$$\dot{m}_{propellant} = A^* \cdot \frac{P_0}{\sqrt{T_0}} \cdot \sqrt{\frac{\gamma}{R_g} \cdot \left(\frac{2}{\gamma+1}\right)^{\frac{\gamma+1}{\gamma-1}}} \quad (11)$$

The combustion products for the gas-specific constant R_g , and ratio of specific heats γ , were calculated using CEA-derived tables of thermodynamic and transport properties. These tables were constructed using the method developed by Whitmore and Peterson⁹ with chamber pressure and O/F ratio as independent variables. For each data point the two-dimensional CEA tables were interpolated using the measured chamber pressure and an assumed mean O/F ratio. The O/F ratio entered into the CEA tables was iterated to produce a fuel mass flow whose integral value exactly equaled the consumed fuel mass measured after each test. The total consumed oxidizer was calculated by integrating the measured Venturi massflow.

VeroClear motor test results

Initially, the VeroClear motors were designed with a plastic injector port directly built into the upper section of the fuel grain holder. During the design phase, it was calculated that isentropic expansion of the oxidizer through this orifice would sufficiently cool the top end of the motor to allow the plastic injector component to survive. Unfortunately, partway through the second burn of the 4-mm motor, the injector port burned out leading to a large pressure spike and automatic features programmed into the control logic shut the motor down. Figure 21 shows the VeroClear motor during the initial test firing. The burning injector can be seen in the glowing section on the left side of motor. Figure 21 also shows a close up of the enlarged injector port following the aborted burn. Even though the motor case itself remained quite cool - less than 20°C - due to the low thermal conductivity of the fuel grain; it is obvious that there is a significant radiation heat load, and the clear material allowed sufficient radiant heat to penetrate the upper end of the motor to melt the plastic injector orifice.

In order to overcome this design flaw, the injector was redesigned by filling the threaded metal inlet fitting with high temperature epoxy, and then drilling out a 1.38mm hole through the cured epoxy. The system was subsequently reprogrammed to burn the motor three successive times, with burn durations of 1, 3, and 5 seconds. Two seconds into the final burn the nozzle failed at the graphite/phenolic insulator interface.

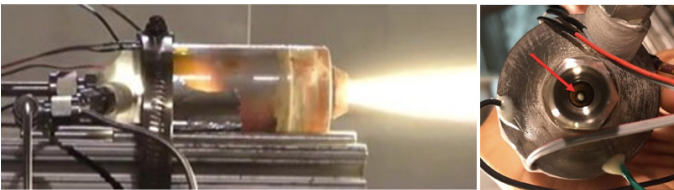


Figure 21 4-mm wall VeroClear motor during startup and at full pressure operation.

Figure 22 shows the resulting thrust and chamber pressure time histories. For first two burns the chamber pressure and thrust levels rapidly rise to the desired steady-state levels of approximately 120 psia and 25 N. On the third and final burn before failure, the chamber pressure never reaches the 120-psia level, indicating that the nozzle retainer had already begun to leak almost immediately after firing. The hot gas blow by between the graphite nozzle and phenolic insulator was almost certainly the cause of the nozzle failure. A follow-on continuous-burn of a second 4-mm VeroClear motor resulted in an identical nozzle failure after 5.5 second. The 2-mm wall thickness VeroClear motor failed in an even worse manner, a successful initial 2.5 sec. burn, followed by a case failure and nozzle ejection 1/2 sec. into the 2nd burn. The aft end of the motor case failed catastrophically, resulting in a forceful ejection of the entire nozzle assembly. Figure 23 shows a picture of the post-test nozzle assembly at the point of the motor case fracture.

These recurring failures indicated a clear deficiency in the nozzle retainer design. A primary cause appears to be the cotton reinforced phenolic used as the nozzle insulator. Following each motor burn the cotton material exposed to the ambient conditions continued to smolder until snuffed. This external burning very likely embrittled and weakened the adhesive used to bond the graphite nozzle at the interface, and contributed to the early failure. Replacing the current insulating material with a flame retardant, graphite-reinforced *Garolite*® or similar insulator would likely prevent this post fire-smoldering issue and increase nozzle survivability.

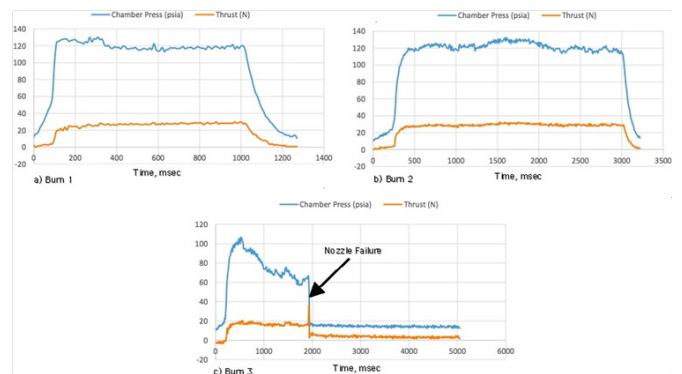


Figure 22 4-mm VeroClear motor, thrust and chamber pressure time histories.



Figure 23 2-mm VeroClear motor, recovered end cap and nozzle assembly.

Nickel plated motor test results

As previously shown by Table 5 only the 16-mil wall thickness nickel-plated motor was hot-fire tested. A total of 5 burns were performed. The total cumulative burn time was slightly greater than 12 seconds. Figures 24 and 25 show representative time history traces the final two burns of the test series (burns 4 and 5). Plotted are a) chamber pressure, b) Thrust, c) Consumed propellant, and d) the total delivered impulse. The thrust level is calculated in two ways, 1) from the thrust stand load cell data, and 2) from the choking massflow calculated by chamber pressure data based on the known nozzle size. On the final burn a 350msec ignition latency observed. This latency was likely due to a char built up inside of the motor ignitor section that insulated the electrodes and made it more difficult for the ignition spark to pyrolyze the fuel. The lagged ignition allowed oxygen to concentrate in the motor and lead to ignition overshoot observed during the first 700msec after ignition.

The observed thrust and chamber pressures are lower for this motor than occurred with the VeroClear motors because of necessary piping changes upstream of the injector. During the nickel-plating process some metal seeped into the motor casing and into close proximity to the ignitor electrodes. Because of this nickel plating, it was feared that there existed a potential for the ignition spark to jump to the test cart. This high-voltage spark - as high as 1000 Volts - has the potential to ruin multiple sensitive instruments. As a mitigation against such an event, the motor was wrapped in silicone rubber before being clamped to the test balance. As a further precaution a section of non-conductive plastic tubing and a back flow valve were inserted between the run valve and the injector.

Table 4 Motor test summary

Motor Configuration	Weight	No. of Burns	Total Burn Time to Failure, sec	Delivered Impulse Before Failure, N-sec	Mean Specific Impulse, sec, Measured (Vacuum)	Mean O/F Ratio	Failure Mode
VeroClear, 4-mm wall Thickness	151	5	8	191.5	225.7 (329.5)	0.95	Nozzle Graphite/ Phenolic Interface
VeroClear, 4-mm wall Thickness	152	1	5.5	121.8	224.8 (322.5)	0.95	Nozzle Graphite/ Phenolic Interface
VeroClear, 2-mm wall Thickness	133	2	3	72.7	218.3 (316)	1.26	Motor Case Failure
Nickel Plated, 16-mil wall Thickness	330	5	12	225	209.5 (329.8)	0.98	No Failures

Table 5 Summary of performance objectives

Performance Objective/Motor Design	Sealed ABS	VeroClear Shell/ABS Grain	Nickel-Plated Shell Shell/ABS Grain
100% Printed Thrust Chamber	✓	✓	✓
Survive Greater than 375 psig Static Load	X	✓	✓
10-25 N Thrust level	--	✓	✓
200 N-sec Total Delivered Impulse	--	✓	✓
12 Seconds Total Burn Life Time	--	X	✓
Multiple Restart Capability Demonstrated	--	✓	✓

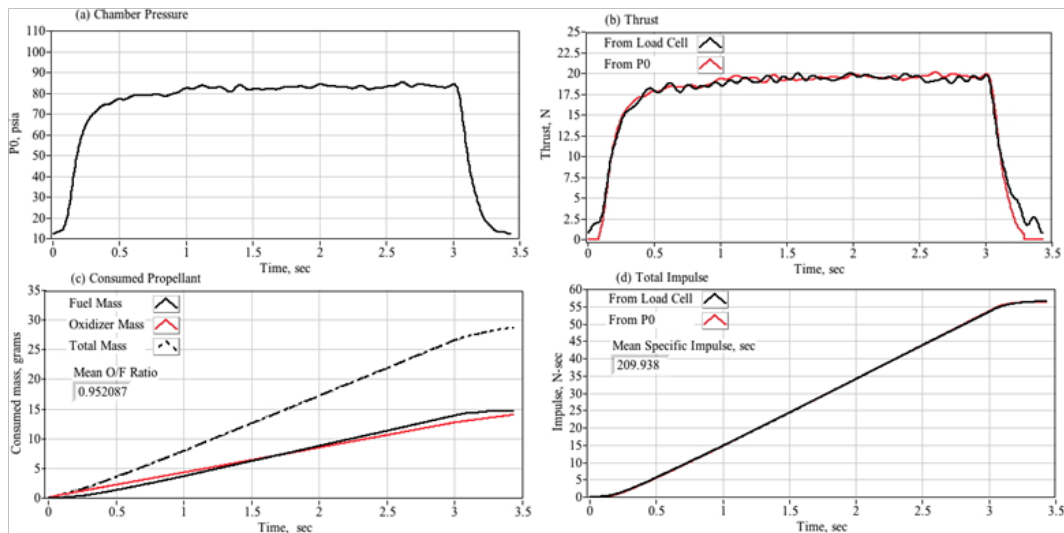


Figure 24 Nickel-motor chamber pressure and thrust time history trace, burn 4.

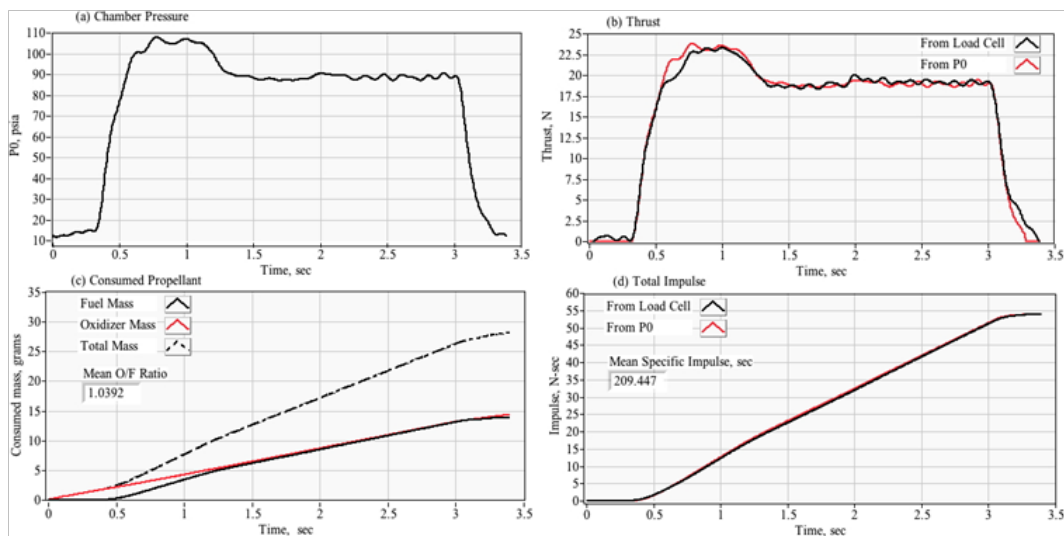


Figure 25 Nickel-motor chamber pressure and thrust time history trace, burn 5.

These additions resulted in an additional 45-50 psig-pressure drop. Because the regulator was already at its maximum outlet setting -350 psig, the pressure loss could not be compensated-for and the lower thrust level resulted. At the end of the 12-second burn lifetime the nozzle retainer was observed to still be quite functional. This difference in survivable burn lifetime is likely due to two factors, 1) the nickel-plating shell that contributed to the overall greater heat capacity of the motor, and 2) the shell opaqueness that insulated the nozzle insulator from a least a fraction of the chamber radiation heating.

The mean longitudinal fuel regression rate was calculated from the fuel mass flow rate by

$$\dot{r} = \frac{\dot{m}_{fuel}}{\rho_{fuel} \cdot 2\pi \cdot r \cdot L_{port}} \quad (12)$$

Rearranging Eq. (12) and integrating up to the current burn time,

$$\int_0^r 2\pi \cdot r \cdot dr = \pi \cdot (r^2 - r_0^2) = \frac{1}{\rho_{fuel} \cdot L_{port}} \int_0^t \dot{m}_{fuel} \cdot dt \quad (13)$$

Evaluating the left hand side and solving for instantaneous fuel port radius

$$r_{(t)} = \sqrt{r_0^2 + \frac{\int_0^t \dot{m}_{fuel} \cdot dt}{\pi \cdot \rho_{fuel} \cdot L_{port}}} \quad (14)$$

The instantaneous cross sectional area of the fuel port is

$$A_{c(t)} = \pi \cdot (r^2 - r_0^2) = \pi \cdot r_0^2 + \frac{\int_0^t \dot{m}_{fuel} \cdot dt}{\rho_{fuel} \cdot L_{port}} \quad (15)$$

and the instantaneous oxidizer mass flux is

$$G_{ox(t)} = \frac{\dot{m}_{ox}}{\pi \cdot r_0^2 + \frac{\int_0^t \dot{m}_{fuel} \cdot dt}{\rho_{fuel} \cdot L_{port}}} \quad (16)$$

Figure 26 plots the mean regression rates calculated from the data of Figs. 24 and 25. Figure 26(a) plots the regression rate time histories during the burn, and Figure 26(b) plots the regression rate against the oxidizer massflux, G_{ox} . In Figure 26(a) the higher regression rate

for burn 4 is substantially higher than the associated rate for burn 5 mainly due to the smaller port radius. When plotted against G_{ox} in Fig 26(b), the two curves merge. Figure 26(b) also plots the exponential least-squares curve fit of the form

$$\dot{r} = a \cdot G_{ox}^n \cdot L_{port}^{n-1} \quad (17)$$

For Eq. (17) G_{ox} is the mean longitudinal oxidizer massflux, averaged over the burn duration. The corresponding curve fit scale and exponent parameters are

$$\left[\begin{array}{l} a = 0.08142 \frac{cm^{1+2n}}{g \cdot sec^{1-n}} \\ n = 0.5021 \end{array} \right] \quad (18)$$

As shown by Karabeyoglu et al.²⁶, for a cylindrical fuel port, the mean longitudinal O/F ratio at any burn time is

$$O/F = \frac{\dot{m}_{ox}}{\dot{m}_{fuel}} = \frac{\dot{m}_{ox}}{\rho_{fuel} \cdot (\pi \cdot D_{port} \cdot L_{port}) \cdot \dot{r}} = \frac{\dot{m}_{ox}}{\rho_{fuel} \cdot (\pi \cdot D_{port} \cdot L_{port}) \cdot (a \cdot G_{ox}^n \cdot L_{port}^{n-1})} \quad (19)$$

Substituting Eq. (17) into Eq. (19) and simplifying gives the result,

$$O/F = \frac{\dot{m}_{ox}}{\rho_{fuel} \cdot (\pi \cdot D_{port} \cdot L_{port}) \cdot \left(a \cdot \left(\frac{\dot{m}_{ox}}{\pi \cdot D_{port}^2} \right)^n \cdot L_{port}^{n-1} \right)} = \frac{\dot{m}_{ox}^{1-n} \cdot D_{port}^{2n-1}}{(4^n \cdot \pi^{1-n} \cdot \rho_{fuel}) \cdot (a \cdot L_{port}^n)} \quad (20)$$

Analysis of Eq. (20) shows that when the burn exponent has a value of $n > 1/2$, the burn is progressive and O/F ratio increases with time as the fuel grain burns and the port opens up. Conversely, when the burn exponent has a value of $n < 1/2$ the O/F burn is regressive and becomes increasingly rich with time. Clearly for a burn exponent with value and $n = 1/2$, Eq. (12) predicts that the burn rate is neutral, implying no O/F shift during the burn. Consequently, based on the curve fit values Eq. (10), as derived from Figure 26, one can conclude that a major pre-design objective of a minimal O/F shift during the burn lifetime was achieved for the Nickel-plated motor configuration. Because of the multiple configuration failures for the VeroClear motors, the burn histories were too erratic to allow a reliable regression rate calculation.

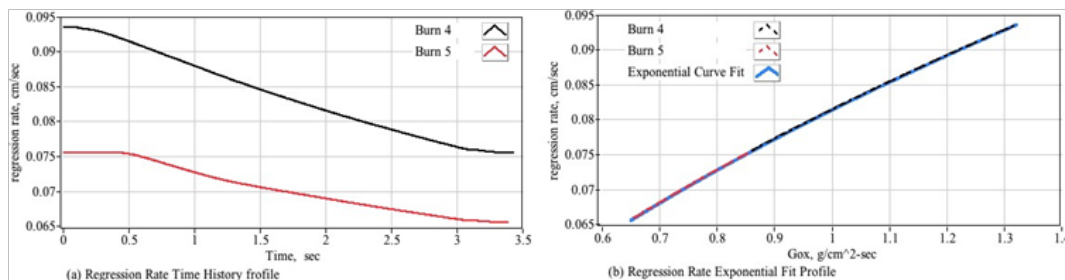


Figure 26 Regression rate calculated from massflow data and corresponding exponential curve fit.

Discussion of results

The simple, inexpensive 3-D printed thruster systems, described herein, has the potential to replace the current generation of spacecraft thruster systems based on hydrazine or solid propellants, for a variety of applications. Of particular interest is the application of the 3-D printed thruster systems as a simple and inexpensive means for actively de-orbiting spacecraft at the end of lifetime (EOL). To date there have been only several hundred small spacecraft and CubeSat launches; however, that number is expected to grow astronomically over the next two decades.²⁸ With that growth, comes a corresponding a significant increase of space debris hazard and the associated risk of

orbital collisions.²⁹ Increasingly, there are calls for active end-of-life measures to de-orbit dead or dying spacecraft.³⁰ In fact, the United National Office for Outer Space Affairs, which establishes Guidelines for the Peaceful uses of Outer Space, has recently released Guideline 6, Space Debris: “Limit long-term presence of spacecraft and launch vehicle orbital-stages in Low-Earth Orbit (LEO) region after end of mission. The Recommendation for the for Time Frame 2025-2030 is: All spacecraft and launch vehicle orbital stages that have terminated operational phases in orbits that pass through LEO should be actively removed from orbit in a controlled fashion.” It is inevitable that these EOL de-orbit guidelines will become mandatory.

Summary and conclusion

This paper presents the design, development, and testing of a unique hybrid rocket system with key components entirely fabricated using additive manufacturing. Three designs were initially considered, 1) a combustor 3-D printed entirely from ABS and sealed using a polymer solvent, 2) a two material combustion chamber assembly fabricated from VeroClear® plastic using PolyJet 3-D SL printing technology, and 3) a motor assembly fabricated from FDM- processed ABS, but plated with an external nickel coating. The all-ABS design was unable to be sealed properly to hold the required pressure levels and was quickly abandoned. Both thick-walled (4mm) and thin-walled (2mm) VeroClear and one thick wall (16-mil) nickel plated ABS design passed the static load testing requirements and were brought forward for hot fire testing. The thick walled Nickel-Plated rocket weighed approximately two times greater than the thick-walled VeroClear-rocket.

Because preliminary analysis showed that isentropic expansion of the oxidizer into the motor case would keep the top end of the motor relatively cool, the VeroClear motors were initially designed with a plastic injector port directly built into the upper section of the fuel grain holder. Unfortunately, radiation heating was significantly larger than anticipated leading to a significant enlargement of the injector port part way through the second burn. In order to overcome this design flaw, the injector was redesigned by filling the threaded metal inlet fitting with high temperature epoxy, and then drilled out to the required injector area.

Following this modification, the 4-mm wall motors was burned three times with programmed burn durations of 1, 3, and 5 seconds. Two seconds into the final burn the nozzle failed at the graphite/phenolic insulator interface. During a second test of an identical version of this motor the nozzle interface failed after 5.5 seconds. The 2-mm wall thickness VeroClear motor failed in an even worse manner, with a catastrophic failure of the motor case aft end approximately 3 seconds after the initial burn.

Because the thin-walled (4 mil) nickel-plated motor failed catastrophically during static-load testing, only the thick wall (16mil) nickel-plated rocket was brought forward for hot fire testing. A total of 5 burns were performed. The total cumulative burn time was slightly greater than 12 seconds. At the end of the 12-second burn lifetime the nozzle retainer was observed to still be quite functional. This difference in survivable burn lifetime is likely due to two factors, 1) the nickel-plating shell that contributed to the overall greater heat capacity of the motor, and 2) the shell opaqueness that insulated the nozzle insulator from a least a fraction of the chamber radiation heating.

Both motor design exhibited specific impulse values near or greater than 210 seconds, with VeroClear design exhibiting slightly higher in the lab specific impulse than did the nickel-plated design, primarily the result of a better- optimized nozzle configuration. During the nickel-plating process some metal seeped into the motor casing and into close proximity to the ignitor electrodes. Because of this nickel plating, it was feared that there existed a potential for the ignition spark to jump to the test cart. This high-voltage spark - as high as 1000 Volts - has the potential to ruin multiple sensitive instruments. Upstream piping changes including a non-conductive tubing section and a check valve caused the Nickel-plated motor to run at approximately 30-psig lower chamber pressures. The extrapolated vacuum specific impulse values for both motors exceeded exceeding 325 seconds.

Fuel regression rates were calculated from the fuel massflow rates for the Nickel-plated rocket burns, and plotted as a function of the

oxidizer mass flux. Exponential curve-fits of the data calculate a burn exponent that is very close to 0.5, a condition that indicates a minimal oxidizer-to-fuel ratio shift during the burn lifetime. Because of the multiple configuration failures for the VeroClear motors, the burn histories were too erratic to allow a reliable regression rate calculation.

The main issue with the overall systems configuration was the only-non-additive component of the combustion chamber design, the nozzle assembly. Even though the nozzle survived the desired 12-second burn lifetime for the nickel-plated rocket design, recurring failures during the hot-fire tests indicated a clear deficiency in the nozzle retainer design. A primary cause appears to be the cotton reinforced phenolic used as the nozzle insulator. Following each motor burn the cotton material exposed to the ambient conditions continued to smolder until snuffed. This external burning very likely embrittled and weakened the adhesive used to bond the graphite nozzle at the interface, and contributed to the early failure. Replacing the current insulating material with a flame retardant, graphite-reinforced *Garolite* or other machinable ceramic insulator would likely prevent this post fire-smoldering issue and increase nozzle survivability.

Even with the identified design issues, the results of this testing campaign are very encouraging. The feasibility of using inexpensive and industry-standard 3-D printing methods to build up thrust chambers with has been demonstrated. Almost no residual material waste occurs using additive methods. Multiple vendors using well- developed commercial technologies can produce identical pieces simultaneously, resulting in a “virtual assembly line.” These manufacturing advantages are not achievable using conventional “machine-shop” fabrication and assembly methods.

There exist multiple opportunities for such inexpensive, green systems to replace existing, very expensive and potentially hazardous, thruster systems for a variety of drop-in applications. Because of their relative simplicity, high performance, and low cost, in the next generation a fully-developed system could be cheaply offered as a stand-alone de-orbit system for commercial payloads. When fully matured this technology is potentially market disruptive, especially for the emerging small spacecraft and CubeSat markets.

Acknowledgments

The author would like to thank Dr. Jonathan Jones and the Marshall Space Flight center for the partial sponsorship of this work through their grant entitled, “Application of Robotic Manufacturing for Hybrid Rocketry Components,” Grant Award Number NNX12AN12G.

Conflicts of interest

Author declares that there is no conflict of interest.

References

1. Rifkin Jeremy. *The Third Industrial Revolution, How Lateral Power Is Transforming Energy, the Economy, and the World*. St. Martens Press LLC: New York; 2011.
2. Fuller JK, Ehrlich DA, Lu PC, et al. *Advantages of Rapid Prototyping for Hybrid Rocket Motor Fuel Grain Fabrication*. 47th AIAA/ASME/SAE/ASEE Joint Propulsion Conference & Exhibit, AIAA Paper 2011-5909; 2011.
3. Arnold D, Boyer JE, Kuo KK, et al. *Test of Hybrid Rocket Fuel Grains with Swirl Patterns Fabricated Using Rapid Prototyping Technology*. AIAA-2013-4141, 49th AIAA/ASME/SAE/ASEE Joint Propulsion Conference: San Jose, CA; 2013.
4. Whitmore Stephen A, Peterson Zachary W, Eilers Shannon D. Comparing Hydroxyl Terminated Polybutadiene and Acrylonitrile Butadiene Styrene as Hybrid Rocket Fuels. *AIAA J Propulsion and Power*. 2013;29(3).

5. Stephen A Whitmore, Sean D Walker, Daniel P Merkley, et al. High Regression Rate Hybrid Rocket Fuel Grains with Helical Port Structures. *AIAA J Propulsion and Power*. 2015;31(6):1727–1738.
6. Stephen A Whitmore. Additively Manufactured Acrylonitrile-Butadiene-Styrene–Nitrous-Oxide Hybrid Rocket Motor with Electrostatic Igniter. *AIAA J Propulsion and Power*. 2015;31(4):1217–1220.
7. Stephen A Whitmore, Nathan Inkley, Daniel P Merkley. Development of a Power-Efficient, Restart-Capable Arc Ignitor for Hybrid Rockets. *AIAA J Propulsion and Power*. 2015;31(6):1739–1749.
8. Whitmore SA. Three-Dimensional Printing of “Green” Fuels for Low-Cost Small Spacecraft Propulsion Systems. *Journal of Spacecraft and Rockets*. 2017;54(6).
9. Whitmore SA, Bulcher AM. *A Green Hybrid Thruster Using Moderately Enriched Compressed Air as the Oxidizer*. AIAA 2018-4841, 2018 Joint Propulsion Conference, AIAA Propulsion and Energy Forum: Cincinnati, OH; 2018.
10. Peterson ZW, Eilers SA, Whitmore Stephen A. *Analytical and Experimental Comparisons of HTPB and ABS as Hybrid Rocket Fuels*. AIAA-2011-5909, 47th AIAA/ASME /SAE/ASEE Joint Propulsion Conference & Exhibit: San Diego CA; 2011.
11. Whitmore Stephen A, Peterson Zachary W, Eilers Shannon D. Comparing Hydroxyl Terminated Polybutadiene and Acrylonitrile Butadiene Styrene as Hybrid Rocket Fuels. *AIAA Journal of Propulsion and Power*. 2013;29(3):582–592.
12. Gordon S, McBride BJ. *Computer Program for Calculation of Complex Chemical Equilibrium Compositions and Applications*. NASA RP-1311; 1994.
13. Marxman G, Gilbert M. Turbulent Boundary Layer Combustion in the Hybrid Rocket. *Symposium (International) on Combustion*. 1963;9(1):371–383.
14. Marxman GA, Wooldridge CE, Muzzy RJ. Fundamentals of Hybrid Boundary Combustion. *Progress in Astronautics and Aeronautics*. 1964;15(1):485–522.
15. Eilers Shannon D, Whitmore Stephen A. Correlation of Hybrid Rocket Propellant Regression Measurements with Enthalpy-Balance Model Predictions. *AIAA J Spacecraft and Rockets*. 2008;45(4):1010–1020.
16. Sutton GP, Biblarz O. *Rocket Propulsion Elements*. 9th ed., Wiley: New York; 2001.
17. Whitmore Stephen A, Merkley Stephen L, Walker Dean D, et al. *A Survey of Additively Manufactured Propellant Materials for Arc-Ignition of Hybrid Rockets*. AIAA 2015-2616, 51st AIAA/ASME/SAE/ASEE Joint Propulsion Conference and Exhibit: Orlando FL; 2015.
18. Whitmore SA, Fehlberg SA. *Direct Electroplating of Additive Manufactured Plastics for Hybrid Rocket Propulsion Systems*. AIAA 2018-4626, 2018 Joint Propulsion Conference: Cincinnati, Ohio; 2018.
19. Gui-xiang W, Ning L, Hui-li H, et al. Process of direct copper plating on ABS plastics. *Applied Surface Science*. 2006;253(2):480–484.
20. Xu W, Zhuang M, Cheng Z. Environmentally Friendly Copper Metallization of ABS by Cu-Catalysed Electroless Process. *Rare Metal Materials and Engineering*. 2016;45(7):1709–1713.
21. Bazzaoui M, Martins JI, Bazzaoui EA, et al. Environmentally friendly process for nickel electroplating of ABS. *Applied Surface Science*. 2012;258(20):7968–7975.
22. Megyesy, Eugene F. *Pressure Vessel Handbook*. 14th ed. PV Publishing, Inc: Oklahoma City; 2008.
23. Daniel Isaac, Ori Ishai. *Elastic Behavior of Composite Lamina-Micromechanics, Engineering Mechanics of Composite Materials*. 2nd ed. New York: Oxford UP; 2006. 49–52 p.
24. Anon Matweb. Nickel.
25. Anon Matweb. Acrylonitrile Butadiene Styrene (ABS).
26. Karabeyoglu A, Toson E, Evans B. *Effect of “O/F Shift” on Combustion Efficiency*. AIAA 2014-3851, AA 284A Advanced Rocket Propulsion. 50th AIAA/ASME/SAE/ASEE Joint Propulsion Conference, AIAA Propulsion and Energy Forum: Cleveland, OH; 2014.
27. Swartwout M. *CubeSat Debris*. Saint Louis University; 2015.
28. NASA Orbital Debris Program Office. *A Review of Space Environment Implications of CubeSat Traffic*. Orbital Debris Quarterly News. 2015;19(3).
29. European Space Agency (ESA). *Position Paper on Space Debris Mitigation: Implementing Zero Debris Creation Zones*. ESA Publications Division, SP-1301: The Netherlands; 2006.
30. Anon. *United Nations Office for Outer Space Affairs, Space Debris Mitigation Guidelines of the Committee on the Peaceful Uses of Outer Space*. Document V09-88517: Vienna Austria; 2010.